Stars and planets at high spatial and spectral resolution

Albrecht, S.

Citation

Albrecht, S. (2008, December 17). *Stars and planets at high spatial and spectral resolution*. Retrieved from https://hdl.handle.net/1887/13359

Chapter 2

A new concept for the combination of optical interferometers and high-resolution spectrographs

The combination of high spatial and spectral resolution in optical astronomy enables new observational approaches to many open problems in stellar and circumstellar astrophysics. However, constructing a high-resolution spectrograph for an interferometer is a costly and time-intensive undertaking. Our aim is to show that, by coupling existing high-resolution spectrographs to existing interferometers, one could observe in the domain of high spectral and spatial resolution, and avoid the construction of a new complex and expensive instrument. We investigate in this chapter the different challenges which arise from combining an interferometer with a high-resolution spectrograph. The requirements for the different sub-systems are determined, with special attention given to the problems of fringe tracking and dispersion. A concept study for the combination of the VLTI (Very Large Telescope Interferometer) with UVES (UV-Visual Echelle Spectrograph) is carried out, and several other specific instrument pairings are discussed. We show that the proposed combination of an interferometer with a high-resolution spectrograph is indeed feasible with current technology, for a fraction of the cost of building a whole new spectrograph. The impact on the existing instruments and their ongoing programs would be minimal.

S. Albrecht, A. Quirrenbach, R. N. Tubbs & R. Vink
AN to be submitted

2.1 Introduction

In recent years optical interferometers have proven that they can produce excellent science in the field of stellar and circumstellar astrophysics. Over the same period high-resolution spectrographs have enabled the discovery of the first extra-solar planets, and contributed substantially to great progress in the field of asteroseismology.

A number of current interferometric instruments have some spectroscopic capabilities. For example the mid- and near-infrared instruments MIDI (The Mid-Infrared instrument, at the VLTI) and AMBER (Astronomical Multiple BEam Recombiner, at the VLTI) provide spectral resolutions of up to $R \sim 250$ and $R \sim 12000$, over bandpasses of ~ 5 μm and ~ 50 nm, respectively. At the CHARA array, the Vega (Visible spEctroGraph and polArimeter) project is under construction with a spectral resolution of $R \sim 30000$ and a bandpass of ~ 50 nm. For science results obtained with spectrally resolved interferometry see for example Vakili et al. (1998) and Weigelt et al. (2007). Unfortunately the combination of very high spectral resolution over a bandpass greater than a few tens of nanometer, to enable a real analog to classical Echelle spectroscopy with interferometric spatial resolution is not yet available.

In building a dedicated high-resolution Echelle spectrograph for an existing interferometer such as the VLTI, one would face several challenges. First of all, building a high-resolution spectrograph is a very costly and time-intensive undertaking. In addition it would be hard to justify building such an instrument only for use with an interferometer, as current optical interferometers are still restricted to very bright objects in comparison with single telescopes. Furthermore, high-resolution spectrographs are usually large instruments, while the space available in the beam combining laboratories of interferometers is often limited. Therefore, it is unlikely that such a dedicated instrument will be built in the near future.

In this chapter we advocate a different approach. By using an existing spectrograph and only building an interface between it and an interferometer at the same site, the combination of high spectral and spatial resolution could be achieved on a much shorter timescale, and for a fraction of the cost of a complete new instrument.

The pre-existing infrastructure would need to consist of two telescopes, delay lines for path compensation, a fringe sensing unit to acquire and stabilize the fringes, and a high-resolution spectrograph on the same site. These conditions are already fulfilled, or will be fulfilled in the very near future, at several observatories. The two most promising sites are:

- In the Southern hemisphere at Paranal Observatory with the VLTI in combination with the UVES spectrograph at Unit Telescope 2 (UT2), or the High-Resolution IR Echelle Spectrometer (CRIRES) spectrograph at UT1.
- In the Northern hemisphere at Mauna Kea with the Keck Interferometer (KI) and HIgh Resolution Echelle Spectrometer (HIRES) at Keck I telescope or the NIRSPEC spectrograph at Keck II. Also at Mauna Kea, the OHANA (Optical Hawaiian Array for Nanoradian Astronomy) interferometer is currently under development, and will allow the combination of several other pairs of telescopes at the Manual Kea site.

In each case, three additional hardware components would be required:

1. A beam combiner that accepts two input beams from the telescopes and feeds the outputs carrying the fringe signals (coded as intensity variations) into fiber feeds;

2. Fibers that connect the interferometer to the spectrograph;
3. A fiber head that feeds the light from the fibers into the spectrograph.

If separate telescopes are available for interferometry (as in the case of the Auxiliary Telescopes of the VLTI), the impact on the single-telescope-use of the spectrograph would be minimal, as it could be used in the interferometric mode during times when other instruments are scheduled for use with the main telescope.

The outline of this chapter is as follows. In Section 2.2 the scientific motivation for the proposed setup will be discussed. Section 2.3 will give an overview of the challenges in designing and building the proposed instrument, and their possible solutions. In Section 2.4 we will give more information about the proposed combination of the VLTI with the UVES spectrograph, and its expected performance. Section 2.5 highlights the main points for other possible interferometer-spectrograph pairings, and Section 2.6 gives our conclusions.

2.2 Scientific case

By taking advantage of the existing infrastructure and instrumentation at the observatories, the proposed interface between a high-resolution spectrograph and an optical / near-infrared interferometer can provide some unparalleled capabilities in a time- and cost-efficient manner. Most importantly, interferometry can be performed with sufficiently high spectral resolution to resolve absorption lines allowing visibility changes across spectral lines to be measured even in late-type stars. The interferometric spectra would also cover a wide wavelength band. Using the broad spectral coverage, one would be able to use cross-correlation techniques to obtain very accurate radial-velocities and line shapes, which have proven extremely helpful in planet search programs and asteroseismology.

Although restricted to observations of relatively bright stars, interferometry at high spectral resolution will provide hitherto inaccessible information on stellar rotation properties, atmospheric structure and surface features, and can have a profound impact on a large number of open questions in stellar astrophysics.

2.2.1 Stellar diameters and limb-darkening

Measuring the variation of the stellar diameter with wavelength, or even better determining wavelength-dependent limb darkening profiles, can provide a sensitive probe for the structure of strongly-extended atmospheres of cool giant stars. Such data can be directly compared with predictions of theoretical models, and provide qualitative new tests of state-of-the-art three-dimensional stellar model atmospheres (Quirrenbach & Aufdenberg 2003). These models make predictions for the emergent spectrum at every point of the stellar disk. To compare model predictions with data from traditional spectroscopy, they have to be integrated over the full disk first. In contrast, interferometric spectroscopy gives access to the center-to-limb variation of the emergent spectrum, and is thus naturally suited to comparisons with model atmospheres.

A first step in this direction has been made with the Mark III and COAST interferometers and with aperture masking, by measuring the diameters of a sample of cool giant stars in filters centered on deep TiO absorption bands and filters in the nearby continuum (Quirrenbach et al.

1993; Tuthill et al. 1999; Quirrenbach 2001; Young et al. 2003). Many stars are found to be substantially larger in the TiO bands, and to have wavelength-dependent asymmetry. It is easy to understand the principle behind these effects: we effectively measure the diameter of the $\tau = 1$ surface of the star, and the height of that surface varies with opacity and therefore with wavelength. In cool stars this variation may be so large (up to $\sim 10\%$ of the stellar diameter for "normal" giants, even more for pulsating variables) that it can be observed as a variation of the effective stellar diameter with wavelength. The higher parts of the atmospheres are cooler, making the brightness distribution across the stellar surface in absorption bands more sensitive to asymmetries in the temperature distribution. The large spectral widths of the filters used for these interferometric observations average over many TiO absorption lines with different strengths. Interferometric high-resolution spectroscopy will provide much more detailed information on the diameter and limb darkening profiles as a function of TiO absorption depth, and thus substantially better constraints on the theoretical models.

Out of the giant stars which have been observed, the variations of the apparent diameter and limb darkening profile with wavelength are most pronounced in Mira stars. The instrument proposed here will enable detailed investigations of the pulsation and wind acceleration mechanisms. Again, high spectral resolution is required to sample a large range of depths in the stellar atmosphere. The advantage of combining high spatial- and spectral-resolution together in one observation of an object rather than using separate observations in this context has also been pointed out by e.g. Wittkowski et al. (2006); Tsuji (2006).

2.2.2 Interferometric Doppler Imaging

Classical Doppler Imaging (DI) has been developed into a very powerful tool (e.g., Rice 2002; Kochukhov et al. 2004). This technique allows mapping of the chemical and magnetic properties of stellar photospheres with surprisingly small details. Up to now, line profiles have been used for DI which are based on average atmospheric structures; this can obviously only be an approximation, in particular in regions of extreme abundance peculiarity. Tools are now available to compute such stellar atmospheres more accurately (e.g., Shulyak et al. 2004), and a reduced abundance contrast between spots and their surrounding is expected. Interferometric high-resolution spectroscopy data will allow a direct check of the models, because abundance analyses can be performed for individual surface regions of prominent chemically-peculiar stars. The same approach is also applicable for other stars with inhomogeneous surface properties, like active cool giant stars, as interferometry allows the study of individual surface regions. The fact that interferometry can isolate the active regions will partly compensate for the lower total signal-to-noise compared to single-telescope spectra, which always average over the whole stellar surface.

2.2.3 Pulsations and asteroseismology

Radial and non-radial stellar oscillations also lead to characteristic surface patterns of line shapes and central velocities. The reconstruction of these patterns from line profile variations alone is plagued with ambiguities, however. These can to a large extent be resolved by the additional phase information contained in interferometric data (Jankov et al. 2002). This means that pulsation modes can be identified uniquely without any need for comparisons with theoretical models. Empirical mode identification with interferometric spectroscopy could become an important tool in the field of asteroseismology (Cunha et al. 2007).

2.2.4 Interpretation of radial-velocity variations

Radial-velocity observations of main-sequence stars have yielded more than 250 planet detections so far. The wealth of information from these surveys has revolutionized the field of planetary system physics, but little is known about the incidence of planets around stars with masses higher than about 1.5 $M_\odot$, because more massive main-sequence stars are difficult targets for radial-velocity observations. Surveys of K giants can provide this information, and planets around such stars have indeed been detected (Frink et al. 2002). Planets in highly eccentric orbits can be easily identified as such in high-precision radial-velocity data due to the distinct shape of the Keplerian velocity variations, but sinusoidal variations observed in a number of objects in ongoing radial-velocity surveys of K giants could be due either to planetary companions or to low-order non-radial g-mode pulsations. It is possible in principle to distinguish between these possibilities by analyzing the line shapes (which should vary along with the radial velocity in the case of pulsations, but remain stable in the case of companions), but this requires very high spectral resolution and signal-to-noise. Observations with interferometric spectroscopy could resolve the stellar disk and hence distinguish more easily between these possibilities, which would help to establish the mass function of planets around stars with masses between 3 and 5 $M_\odot$. Similar arguments apply to other cases in which radial-velocity variations could plausibly be attributed to different mechanisms, either related to stellar variability or to companions.

2.2.5 Cepheids and distance ladder

Limb darkening curves measured for a spectral line can provide direct measurements of the projection factors of Cepheid pulsations, which relate the true velocity of the pulsation to the observed radial-velocity curve. Uncertainties in this “p factor”, which presently must be computed from theoretical models, are a serious limiting factor in current estimates of Cepheid distances with the Baade-Wesselink method (Sabbey et al. 1995; Marengo et al. 2002; Nardetto et al. 2006). Interferometric spectroscopy can thus eliminate one of the important contributions to the error budget for distances to Cepheids and other variable stars.

2.2.6 Orientation of stellar rotation axes

Stellar rotation induces a difference in the fringe phase between the red wings and the blue wings of stellar absorption lines in resolved interferometric observations. Measuring the position angle of the phase gradient allows determination of the orientation of the stellar axis on the sky (Petrov 1989; Chelli & Petrov 1995). More detailed modeling of the interferometric signal can also provide the inclination of the stellar rotation axis (Domiciano de Souza et al. 2004). High resolution spectroscopy will thus open a way to determine the orientation of stellar rotational axes in space.

To know the orientation of the stellar axes in space is of particular interest in double- or multiple-star systems. One can determine whether the rotation axes of binaries are aligned with each other, and with the orbital rotation axes of the systems. The orientation of the rotational axes contains information about the origin and evolution of the system (see also Chapters 4 and 5).

One can also search for (partial) alignment of rotation axes in star forming regions and stellar clusters. Interactions between stars in multiple systems and other stars in a stellar cluster change the momentum of the systems.

The orientation of the stellar rotation axes will be of special interest for stars which harbor planets, since the mutual inclination between the orbital plane of the companion and the rotation axis of the star can provide insights into the formation and evolution processes of the planet. If the orbital evolution of planetary systems is dominated by few-body scattering processes, or Kozai migration, one might expect to find orbits that are not aligned with the stellar angular momentum (e.g., Lin & Ida 1997; Papaloizou & Terquem 2001; Wu & Murray 2003; Nagasawa et al. 2008). In the near future, astrometric orbits will become available from ground-based and space-based astrometry with the Phase-Referenced Imaging and Micro-arcsecond Astrometry (PRIMA) facility at the VLTI, the Space Interferometry Mission (SIM), and with GAIA. Combining this information with interferometric high resolution observations will provide the relative inclination between the orbital and equatorial plane for a large number of planets in a variety of orbits.

2.2.7 Differential stellar rotation

Along with the oscillation spectrum, differential rotation is a powerful diagnostic for the interior structure of a star. Unfortunately, observations of differential rotation are difficult with classical spectroscopy, and degeneracies exist between inclination, limb darkening, and differential rotation (e.g., Gray 1977). These degeneracies can be resolved by the additional information from interferometric spectroscopy (Domiciano de Souza et al. 2004). High spectral resolution is of the essence for this application, giving the proposed type of instrument a big advantage over more conventional interferometric spectrographs such as AMBER.

2.2.8 Circumstellar matter

Velocity-resolved interferometric observations of emission lines can be used to determine the structure and velocity field of disks around pre-main-sequence objects and Be stars (e.g. Quirrenbach et al. 1997; Young et al. 2003; Tycner et al. 2006; Meilland et al. 2007). It is possible to determine the disk opening angle and the rotation law in the disk, to measure the location of the inner edge of the disk, and to obtain detailed information on possible asymmetries caused by spiral waves. Interferometric observations of winds and outflows from pre-main-sequence stars and from evolved objects can be used to determine their extent and overall geometry, and to probe sub-structure such as clumps and shells. These observations will not need the full spectral resolution offered by high-resolution optical spectrographs, but access to the Hα line is of critical importance.

2.3 Instrument and infrastructure

In this section we describe our proposal for combining an optical/IR interferometer with a high-resolution spectrograph. Figure 2.1 shows a schematic drawing of the combined instrument, while a possible design for the beam combiner is shown in Figure 2.2. Special attention is given to longitudinal dispersion compensation (Section 2.3.2). This has to be addressed if one wants to perform long integrations (several minutes) over a wide bandpass, one of the key abilities of the proposed instrument.

2.3.1 Telescopes

The Earth's atmosphere distorts planar incoming wavefronts from an unresolved astronomical source, introducing phase fluctuations as a function of position and time (Roddier 1981). These fluctuations are commonly described by a Kolmogorov spectrum (Tatarski 1961; Kolmogorov 1941) with constant Fried parameter r_0 (Fried 1966). In order to obtain stable complex visibilities, the incoming stellar wavefronts at the beam combiner have to be flat (with constant wavefront phase as a function of position in the pupil plane for an unresolved star). This can be achieved using either:

1. telescope aperture diameters small enough that the atmospherically-induced phase variations are negligible with $D/r_0 \leq 1$ (this may require a variable pupil stop);
2. tip-tilt correction making wavefront errors negligible on aperture diameters up to $D/r_0 \simeq 3$; or
3. higher-order adaptive optics.

Larger apertures can be used at longer wavelengths or under better seeing conditions, as the Fried parameter varies as $r_0 \propto \lambda^{6/5}$ and $r_0 \propto 1/\mathrm{FWHM}_{seeing}$ for observations at a wavelength λ and with a seeing disk of FWHM_{seeing}.

2.3.2 Longitudinal dispersion compensation

To compensate for the difference in path length from the two telescopes to the source, optical path must be added to one arm of the interferometer. This is typically achieved through the use of *optical trombone* delay lines or through the stretching of optical fibers (Monnier 2003). If the optical delay compensation is performed in a dispersive medium, the Optical Path Difference (OPD) where the fringes are found will vary with wavelength. Longitudinal dispersion can affect the OPD in the proposed instrument concept in two ways:

1. Dispersion will give a variation of optical delay across the wavelength range of the spectrograph;
2. If the spectrograph operates in a different waveband from the fringe tracker, dispersion will introduce a different OPD in the spectrograph waveband to that in the fringe-tracking waveband.

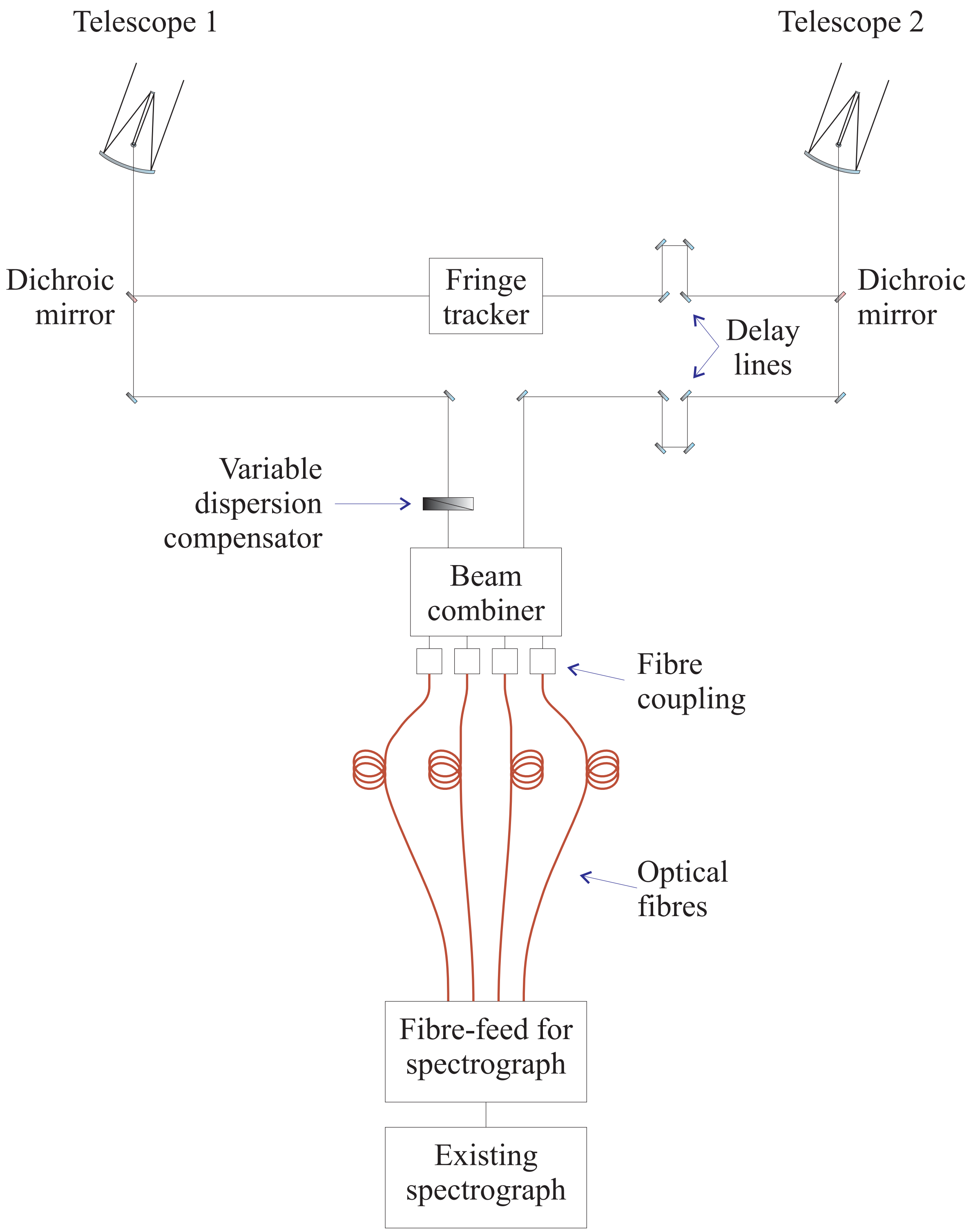

Figure 2.1 — Schematic of the combined instrument, interferometer and spectrograph. The proposed instrument relies on pre-existing infrastructure (telescopes, fringe-tracker, delay lines and a spectrograph located within a few hundred meters). The additional components which must be built include the variable dispersion compensator, beam combiner, fiber coupling, optical fibers and fiber-feed for the spectrograph.

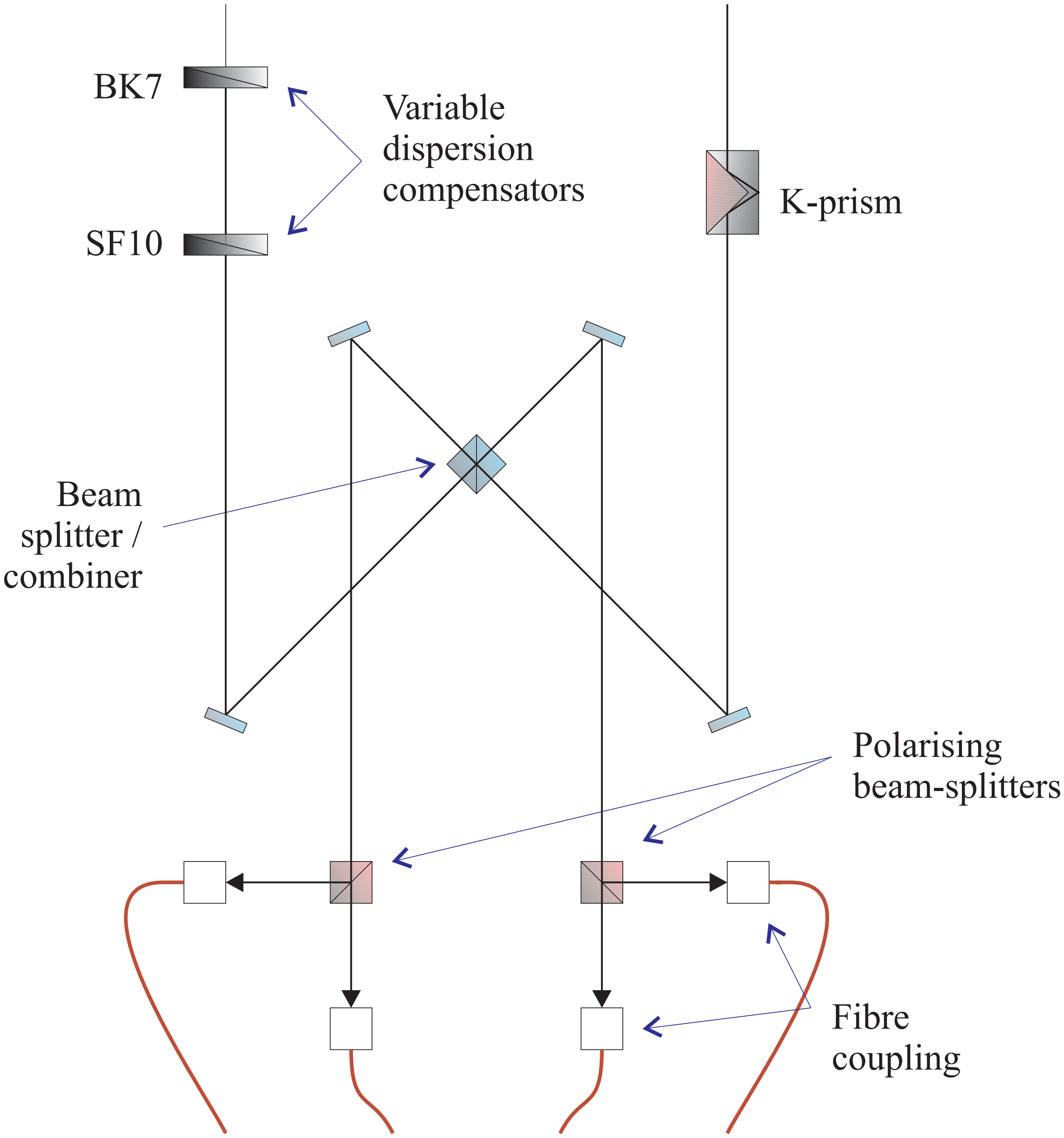

Figure 2.2 — Schematic of the suggested beam combiner for the coupling of a spectrograph to an interferometer. The beam from one telescope passes through a K-prism which introduces an achromatic phase shift of $\pi/2$ between the s and p polarizations. The beam from the other telescope passes through longitudinal dispersion compensators. The combination of the two beams in the beam-splitter introduces a phase shift of π between the two output beams. The two polarizations of the two output beams are separated by the polarizing beam-splitters, resulting in four beams with phase relations of 0, $\frac{\pi}{2}$, π, $\frac{3\pi}{2}$ entering the fibers.

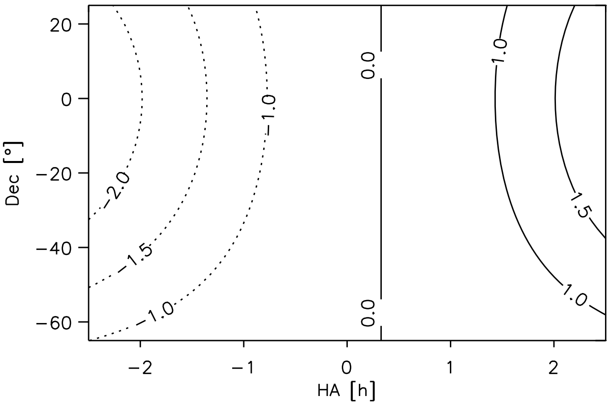

Figure 2.3 — Change (in m) of OPD during a 10 minute integration as a function of HA and Declination for the G1-J6 AT stations at the VLTI which form a baseline of a length of 192 m and an orientation angle of $-2°$. An angle of $0°$ would indicate a baseline directed towards the North.

For a typical high-resolution spectrograph the coherence length of the fringes in each spectral channel is much larger than the optical delay offsets introduced by dispersion. However, time-variation of the dispersion effects during a spectrograph detector integration will blur the interference fringes, reducing the measured visibility amplitude. The two principal sources of variation in optical delay due to dispersion are:

I During an observation the position of the object on the sky changes. To keep the interference fringes at a stable position, the additional optical path introduced in one arm of the interferometer must be varied as the Earth rotates. The change in optical path through the dispersive medium in one arm of the interferometer causes the visibility phase to vary differently at each wavelength. During the course of an observation of several minutes this inevitably leads to a loss of fringe contrast for observations in a waveband of non-zero bandwidth. For example, during a 10-minute visible-light integration, the geometric delay path can change by several meters (see Figure 2.3 and Figure 2.4), which would lead to a relative OPD shift of several μm between R band and I band.

II A change in the temperature or humidity of the air in one of the optical paths to the star will introduce a change in the column density of air and/or water vapor. To first order, these changes will be corrected by the fringe tracking. The residuals are not expected to be large enough to give different delays for different spectral channels in the spectrograph bandpass. However, if the spectrograph is operating in a different waveband from the fringe tracker, the optical delay in the spectrograph waveband may differ from that in the fringe tracking waveband.

Both dispersion problems could be circumvented by restricting the exposure time, but this would reduce the observational efficiency, and in the read-noise limited regime it would reduce the limiting magnitude. Reducing the spectral bandwidth would solve point I above, but would limit the spectral coverage of the observations. As one can see in Figure 2.3 and Figure 2.4, the change in OPD depends on the declination of the star and on the alignment of the baseline with the rotation axis of the earth. Therefore, restricting the baseline geometry and restricting the selection of sources would also circumvent point I above. This would seriously reduce the usefulness of the proposed instrument.

A better way to address point I above would be to equip the beam combiner with a variable atmospheric dispersion compensator (see e.g. Section 2.4.3). This dispersion compensator

Figure 2.4 — Same as Figure 2.3, but this time with a baseline of 109 m length and an angle of 88° (C1-J2).

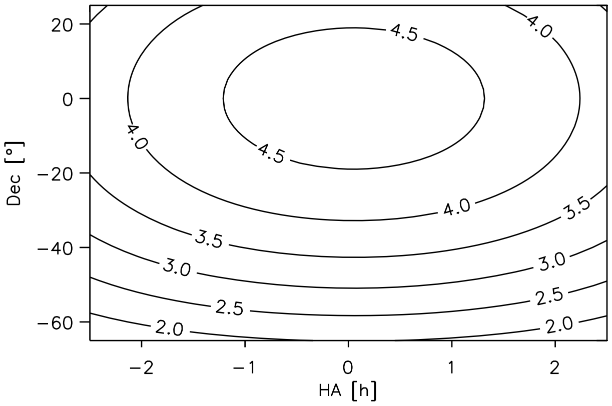

would correct for the differential dispersion introduced by the few meters of additional path between the two telescopes added during the course of the observations; it does not need to correct for the full differential air path.

Point II can be addressed by estimating the dispersion at the wavelength of the spectrograph using measurements of the ambient environmental conditions (Albrecht et al. 2004) and the variation of optical delay with wavelength across the fringe-tracking bandpass. If the fringe tracker cannot operate sufficiently far from the zero optical group-delay point, then an additional delay line will be required in order to provide a different geometrical delay for the spectrograph than is used for light that is sent to the fringe tracker, as shown in Figure 2.1.

2.3.3 Fringe tracker

The proposed instrument scheme relies on the interferometer having a fringe-tracking capability. The fringe tracking must keep the fringes of the spectroscopic observation stable even if they are observed at a different wavelength to the one used for fringe tracking. The fringes in the spectroscopic instrument must be kept stable to a fraction of a wavelength (typically ~ 1 rad of visibility phase). A number of existing interferometers already have fringe-tracking instruments (Delplancke 2003; Colavita et al. 2004; McAlister et al. 2004). The RMS noise (the jitter) in the optical delay from the fringe tracking will cause a reduction in the visibility amplitude by a factor γ:

$$\gamma = \exp\left(-2\left(\frac{\pi\sigma_d}{\lambda}\right)^2\right) \tag{2.1}$$

where σ_d is the RMS variation in the optical delay compensation in a spectral channel with wavelength λ during a detector integration.

2.3.4 Beam Combiner

The primary observable in an interferometer is the complex visibility (having amplitude and phase), proportional to the complex coherence function of the radiation received by the two telescopes (Quirrenbach 2001). The complex visibility can be derived in a number of ways, for example using a fixed delay offset and measuring the fringe signal as a function of wavelength in the spectrum (Labeyrie 1975). Alternatively, to obtain the full information on the complex visibility in each spectral channel, one can measure the four fringe quadratures at each wavelength, i.e. measure the light intensity with fringe phase offsets of 0, $\pi/2$, π and $3\pi/2$ radians. The normalized light intensities as a function of wavelength λ in these four outputs are commonly called $A(\lambda)$, $B(\lambda)$, $C(\lambda)$, and $D(\lambda)$ respectively. The $A(\lambda)$, $B(\lambda)$, $C(\lambda)$, and $D(\lambda)$ outputs can be produced using 50% beam-splitter(s) (providing a π phase shift between the output beams) and achromatic $\pi/2$ phase shifts in two of the four output beams (see e.g. Figure 2.2). The complex visibility $V(\lambda)$ in the spectral channel at wavelength λ is then fully described by the four intensities $A(\lambda)$, $B(\lambda)$, $C(\lambda)$, and $D(\lambda)$:

$$\begin{aligned} V(\lambda) = {} & 2 \cdot \frac{A(\lambda) - C(\lambda)}{A(\lambda) + B(\lambda) + C(\lambda) + D(\lambda)} \\ & + 2i \cdot \frac{B(\lambda) - D(\lambda)}{A(\lambda) + B(\lambda) + C(\lambda) + D(\lambda)}, \end{aligned} \tag{2.2}$$

where $i = \sqrt{-1}$.

The squared amplitude of this visibility estimate $|V(\lambda)|^2$ and the argument (fringe phase) $\phi(\lambda)$ are given by:

$$\begin{aligned} |V(\lambda)|^2 &= 4 \cdot \frac{(A(\lambda) - C(\lambda))^2 + (B(\lambda) - D(\lambda))^2}{(A(\lambda) + B(\lambda) + C(\lambda) + D(\lambda))^2}, \\ \phi(\lambda) &= \arctan \frac{A(\lambda) - C(\lambda)}{B(\lambda) - D(\lambda)}. \end{aligned} \tag{2.3}$$

Applying the fringe estimators on a wavelength-by-wavelength basis, one can thus derive the complex visibility as a function of λ.[1]

The absolute phase will usually be corrupted by turbulence in the Earth's atmosphere, but differential phases can be measured between adjacent spectral channels or between the fringe tracking wavelength and one of the observed spectral channels. These differential phases can provide very valuable observables, such as phase differences between the red and blue wings of spectral lines. In sources which are resolved in some spectral lines but which are un-resolved at continuum wavelengths (e.g. Be stars, as discussed in Section 2.2.8), the complex visibilities can be used to make interferometric images of the structure in the spectral lines, using the position of the unresolved continuum source as the phase reference. In this context it is worth noting that phenomena on scales much smaller than the 'resolution limit' λ/B of the interferometer with baseline B are accessible with this technique, because differential phases with a precision of a few degrees provide astrometric accuracy significantly higher than the conventional (imaging) resolution limit.

---

[1] Note that the estimator for $|V(\lambda)|^2$ in Eqn. 2.3 is biased — $|V(\lambda)|^2$ will be over-estimated in the presence of noise. Slightly modified estimators can be used to give unbiased estimates of $|V(\lambda)|^2$ (e.g., Shao et al. 1988).

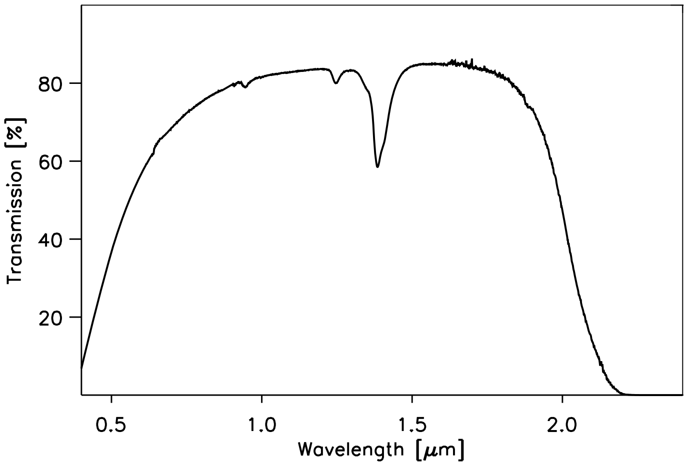

Figure 2.5 — Transmission in the wavelength range from 0.4 to 2.5 μm for 150 m of Optran Plus WF fiber (Ceramoptec catalog, see http://www.ceramoptec.com/catalog.htm).

2.3.5 Connection to the spectrograph

The outputs from the beam combiner can be easily transported to the spectrograph using multimode fiber optics. Only the light intensity as a function of wavelength is of interest at this point (after beam combination), so the additional optical path length and longitudinal dispersion from the fiber are unimportant.

For a link at visible or near-infrared wavelengths one could for example use the Optran Plus WF fiber with a core diameter of 100 μm (see Figure 2.5). Fluoride glass fibers could provide better throughput at longer near-infrared wavelengths.

The insertion of pick-off mirrors might provide a good solution for directing the light from the fibers into the spectrograph. However, in some infrared slit spectrographs, the slit is located in a cryogenic part of the instrument. If it is undesirable to make modifications inside the cryogenic Dewar, it may be sufficient to place the fibers in an image plane outside the spectrograph Dewar.

If the spectrograph is already a fiber-fed instrument, the number of new components will be small and the installation fast.

2.4 An illustrative example: UVES-I

In this section we investigate in more depth the possible combination of the VLTI interferometer with the UVES spectrograph. We name this combination *UVES-I* in the reminder of this chapter. In particular we address here the matter of external fringe tracking and dispersion compensation in Sections 2.4.2 and 2.4.3, respectively. As mentioned above it is essential to solve these points if one wants to combine a high-resolution Echelle spectrograph like UVES with an optical interferometer like VLTI and carry out long exposures, which has not been done so far.

2.4.1 VLTI Auxiliary Telescopes

UVES-I would operate in the wavelength range between 0.6 μm and 1.0 μm. Therefore it would use the VLTI ATs (1.8-m Auxiliary Telescopes) and not the UTs (8-m Unit Telescopes) as the Multi Application Curvature Adaptive Optics (MACAO) adaptive optics systems of the UTs do not deliver well-corrected wavefronts in the visible.

The existing tip-tilt correction on the ATs would allow the use of $3r_0$ sub-apertures with UVES-I (corresponding to ~ 75 cm at 800 nm under typical seeing conditions). With the planned installation of adaptive optics systems at the ATs, their full 1.8 m apertures would become useable for UVES-I, corresponding to a sensitivity gain of ~ 2 mag.

The ATs currently have a dichroic beam-splitter sending the visible light to the tip-tilt system, and passing the infrared light to the delay lines and instruments. This beam-splitter reduces the VLTI transmission in the visible considerably (Puech & Gitton 2006). For UVES-I this dichroic should be replaced by 10-90 beam-splitter, with only 10% of the visible light used for tip-tilt correction. The astronomical targets of interest are all bright enough that they will still give good tip-tilt performance. The sensitivity estimates given in Section 2.4.6 are based on this change, and assume a total VLTI transmission of 6% (Puech & Gitton 2006).

2.4.2 Fringe tracking with PRIMA

Starlight at wavelengths longward of 1.5 μm will be separated using a dichroic mirror and sent to the PRIMA fringe tracker (see Figure 2.2) for stabilization of the fringes. If the R-band fringes at the beam combiner can be stabilized to less than one radian of fringe phase long integrations ($\gg$ than the atmospheric coherence time) can be performed. In order to stabilize the fringe phase at R-band, the OPD at R-band must be calculated from the measured environmental conditions in the VLTI and the measured phases in the PRIMA spectral channels (1.95–2.45 μm).

For the case of von Karman turbulence (Goodman 1985) with finite outer scale L_0, the spatial structure function for the optical phase D_Φ asymptotically approaches a maximum value of $D_\Phi(\infty)$ (Lucke & Young 2007):

$$D_\Phi(r) \equiv \left\langle \left|\Phi(r') - \Phi(r'+r)\right|^2 \right\rangle \rightarrow D_\Phi(\infty), \text{ as } r \rightarrow \infty \tag{2.4}$$

For von Karman turbulence, Lucke & Young (2007) give a possible range of:

$$0.0971 \left(\frac{L_0}{r_0}\right)^{5/3} < D_\Phi(\infty) < 0.173 \left(\frac{L_0}{r_0}\right)^{5/3} \tag{2.5}$$

The total contribution of seeing to OPD fluctuations is typically estimated by assuming that the seeing is caused by a wind-blown Taylor screen of frozen turbulence passing the interferometer array telescopes at a velocity v (Taylor 1938; Buscher et al. 1995). Under this assumption, the asymptotic value of the temporal structure function will be equal to the asymptotic value of the spatial structure function:

$$D_\Phi(t) \equiv \left\langle \left|\Phi(t') - \Phi(t'+t)\right|^2 \right\rangle \rightarrow D_\Phi(\infty), \text{ as } t \rightarrow \infty \tag{2.6}$$

For a typical value of $r_0 = 0.25$ m at 800 nm wavelength and $L_0 = 22$ m (Martin et al. 2000) this would lead to a mean-square optical phase variation $D_\Phi(\infty)$ of:

$$170 \text{ radians}^2 < D_\Phi(\infty) < 300 \text{ radians}^2 \quad (2.7)$$

For a two-telescope interferometer with a long baseline, the mean-square variation in fringe phase will be up to twice as large. As this corresponds to fringe motions of several wavelengths, active fringe tracking will be required in order to perform long integrations.

The OPD fluctuations caused by astronomical seeing can be split up into two constituent parts:

1. variations in the mean particle density due to temperature fluctuations (temperature seeing, with no change in the air composition); and

2. replacement of dry air with an equal particle density of water vapor (water vapor seeing, with no change in particle density).

Measurements using the MIDI 10 μm instrument at the VLTI indicate that the differential column density of water vapor typically varies by an RMS of $\lesssim 1$ mole m^{-2} (Meisner 2007) due to water vapor seeing (the displacement of dry air by an equal particle density of water vapor). This introduces a mean-square fringe phase fluctuation of up to 50 rad^2 at 800 nm wavelength. The remaining 290–600 rad^2 of mean square phase variation result from temperature seeing[2].

If fringe tracking is performed at K-band, the fringes will be partially stabilized in R-band and I-band. Figure 2.6 shows plots of the refractivities of dry air and water vapor, normalized to unity at a fringe-tracking wavelength of 2.2 μm. The black *dry air* curve shows the relative amount of OPD at each wavelength if temperature seeing in a dry-air atmosphere introduced 1 unit of OPD at 2.2 μm. For air of finite humidity, the plot of the relative amount of fringe motion would be shifted linearly a small amount ($< 1\%$ of the way) towards the blue *water vapor* curve.

If the geometrical path length is varied in order to stabilize the fringes at K-band against temperature seeing, and no additional compensation is applied to account for the different refractivity in the visible, the correction applied will be 0.5–1.5% too small to stabilize the fringes between 600 and 900 nm. For the 288–602 radians^2 of mean square phase variation expected from temperature seeing, this will lead to an RMS fringe-tracking error of 0.1–0.4 radians at 800 nm wavelength.

The red curve in Figure 2.6 shows the relative effect of water vapor seeing at different wavelengths. It corresponds to the difference in refractivity between air and water vapor of the same (low) density, with the curve normalized to be unity at 2.2 μm (the fringe-tracking wavelength). A mean-square fringe phase fluctuation of $\simeq 50$ radians^2 due to water vapor seeing at 800 nm wavelength will correspond to $\simeq 0.90$ μm RMS motion at 800 nm wavelength, but from Figure 2.6 it can be seen that the fringe motion due to the water vapor seeing will always be 15% larger at 2.2 μm. If K-band fringe tracking is performed with no compensation for the different air refractivity in the visible, this will introduce an RMS residual of $\simeq 1$ radian to the

---

[2] A small fraction of the water vapor column density fluctuations is expected to occur within the VLTI, but this can be ignored when estimating the atmospheric contribution to the temperature seeing.

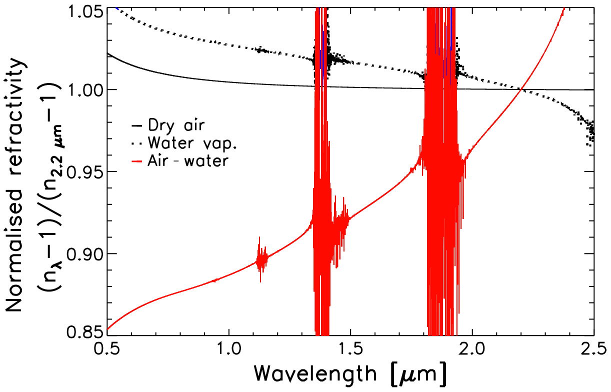

Figure 2.6 — Normalized refractivities of air and water vapor, plotted in black and blue respectively. The refractivity (equal to $n-1$ where n is the refractive index) is plotted against wavelength for dry air and water vapor. The refractivity curves have been normalized in this plot such that the refractivity value at 2.2 μm is unity. Also plotted in red is a curve of the refractivity of dry air minus the refractivity of water vapor, which has been normalized in the same way. The normalization process stretches this curve vertically. The data were taken from Ciddor (1996) and Mathar (2004)

fringe phase at 800 nm wavelength. This would cause a reduction of the fringe visibility due to blurring of the fringes in long exposures.

The approach described by Meisner (2007) for N-band fringe stabilization using PRI-MA can be adapted to improve R- and I-band fringe stabilization during fringe phase tracking. In this method, the geometric path from the star and the differential column density of dry air are estimated from the position of the optical delay lines and measurements from environmental sensors in the VLTI (Albrecht et al. 2004). The K-band group phase measurements provided by the PRIMA instrument are only very weakly dependent on the differential column density of dry air, but are strongly dependent on the differential column density of water vapor. If the effect of the estimated dry-air column density is subtracted from the measured group phase, the resulting group phase can provide a good estimate of the water vapor column density. The fluctuations in the measured water vapor column density can then be used to calculate and independently correct the residuals produced by water vapor and dry air seeing, assuming that the drift in the geometric delay error is small during one integration.

Analyses of temperature, pressure and absolute humidity data taken on 4 nights immediately following the installation of the four humidity and temperature sensors at Paranal (Albrecht et al. 2004) show that the square root of the temporal structure function of the density of air molecules typically varies by less than 0.003 moles m^{-3} (see Figure 2.7) at all measured locations within the VLTI, during a 2-minute integration. There is no measurable correlation between the fluctuations in the different ducts to the telescopes and the fluctuations in the main delay tunnel on timescales of a few minutes. The observed water vapor fluctuations within the VLTI are less than 3×10^{-4} moles m^{-3} over a 2-minute integration, and are already included in the $\lesssim 1$ mole m^{-2} figure from Meisner (2007).

In the extremely pessimistic case that all the air in an entire 100-m duct simultaneously undergoes the same 0.003 moles m^{-3} density change, 2 μm of OPD would be introduced at a wavelength of 2.2 μm. The light paths at the VLTI pass through two such ducts and through an air-filled main delay line, but the total OPD fluctuation due to density changes within the

Figure 2.7 — Square root of the temporal structure function of the dry air density at two locations in the VLTI for the Night 22/23 September 2004. The solid line shows the temporal structure function for measurements at the M16 mirror in front of the interferometric laboratory, and the dashed line displays the same measurements inside the light duct towards the UT 4 telescope.

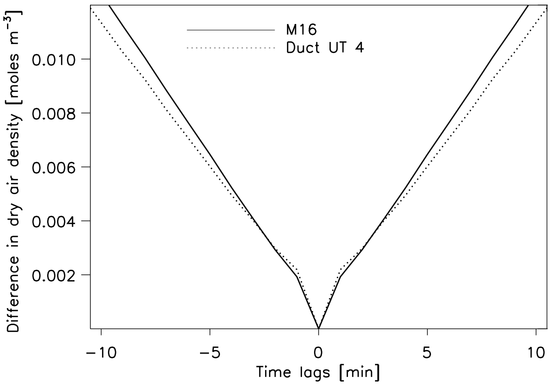

VLTI is still expected to be much smaller than the figure of 24–33 μm RMS OPD estimated above for temperature seeing in the atmosphere. The measurements of K-band fringe phase and group phase include the complete path through the atmosphere and instrument as far as the PRIMA optical bench, so OPD fluctuations caused by changes in the ambient conditions within the VLTI will be accurately tracked.

The expected fringe tracking noise introduced by the PRIMA instrument itself will be 100 nm for a star with $m_K = 8$, and 50 nm at $m_K = 6$ (see Figures 5-12 of Delplancke (2003), and Tubbs et al. (2007)). Equation 2.1 gives visibility losses of 27% and 7.5% respectively at 800 nm, which is easily tolerable.

2.4.3 Dispersion compensation for UVES-I

Each meter of unbalanced air path introduces (under median Paranal atmospheric conditions) offsets from the K-band group delay zero-point of 108 nm and 412 nm, respectively, for the fringes at 900 nm and 600 nm wavelength. This fringe motion can be accurately predicted from environmental sensor measurements and the known geometrical delay. It can be stabilized at one wavelength using a delay line, but to give good stabilization over the full 900 nm to 600 nm wavelength range, a variable dispersion corrector is required.

Starlight at wavelengths shorter than 1.5 μm is separated from the K-band fringe tracking light by a dichroic mirror into the dispersion compensator. The dispersion compensator and the beam combiner are located on the same optical table as PRIMA to ensure alignment and OPD stability (see Figure 2.2).

Viable solutions for a single-material dispersion compensator exist. Using data from the Schott catalog (http://us.schott.com/sgt/english/products/listing.html), the Sellmeir dispersion formula (e.g. Berger et al. 2003), and Cramer's rule we find that, for the 0.6-μm to 1-μm wavelength range SF10 glass can be used (see Figure 2.8, upper panel). For extreme parameters — a build up of 10 m delay during integration, compare also to Figures 2.3 and 2.4 — the residual uncompensated optical path length would reach 150 nm, however; therefore an arrangement where two different materials are used for the dispersion compensation is preferred. A combination of fused silica and BK7 glass gives the best theoretical performance, but the required glass thickness is relatively high (see Figure 2.8, lower panel). We therefore favor a SF10/BK7 combination, which provides compensation to 70 nm even for extreme delay rates, using much thinner glass elements (see Figure 2.8, middle panel). The variable dispersion compensator will also compensate for the fixed additional dispersion produced in the K-prism.

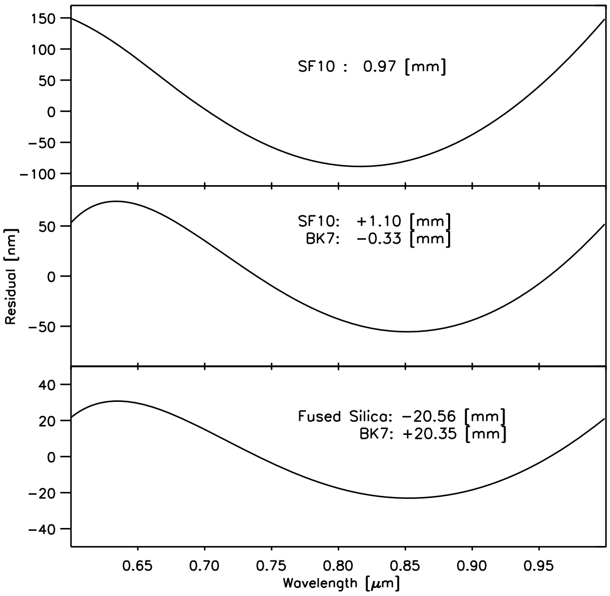

Figure 2.8 — Residual dispersion after accumulation of a 10 *m* change of the total delay, using atmospheric dispersion compensators made of: a] SF10; b] SF10/BK7; and c] BK7/Fused Silica. The combination of SF10 and BK7 (b]) could be used for an instrument like UVES-I. The thickness of the material needed for the compensation is also indicated. For example an additional air path of 10 m in one beam would require the insertion of a 0.97 mm SF10 glass in the other beam.

In addition to the compensation of the delay differences in the visible band, we must also compensate the delay difference between the visible band and the K-band, where PRIMA tracks the fringes. This can be done by commanding the PRIMA fringe tracker to fringe track far enough from the K-band group delay zero point to allow compensation of the fringes at visible wavelengths, or alternatively by inserting another additional delay as shown in Figure 2.1.

2.4.4 Beam combiner for UVES-I

One beam is sent through an achromatic phase shifter (e.g. K-prism), which introduces a $\pi/2$ phase shift of one polarization state with respect to the other. Variable dispersion compensation is applied in the other beam. The dispersion introduced by the K-prism is also compensated in the dispersion compensator. Two flat mirrors then direct the beams into the main beam combiner (Figure 2.2). The combined beams, which have a phase shift of π relative to each other, are sent to polarizing beam-splitters by a second pair of flat folding mirrors (see Figure 2.2). The polarizing beam-splitters separate the two linear polarizations (with their $\pi/2$ phase differences) giving the four fringe quadratures $A(\lambda)$, $B(\lambda)$, $C(\lambda)$, and $D(\lambda)$.

Full information on the complex visibility can be obtained from the four fringe quadratures $A(\lambda)$, $B(\lambda)$, $C(\lambda)$ and $D(\lambda)$ as discussed in Sect. 2.3.4. For an ideal beam combiner, the complex visibility can then be calculated for each spectral channel using Eqn. 2.2.

The requirements on the precision of the phase shift are rather loose; one can easily tolerate up to 10° errors as long as they are stable. Errors in the phase shifts can be compensated for in software, using a similar approach to that used for phase measurements with the PRIMA instrument (Tubbs et al. 2007). Similarly, there are no stringent requirements on the splitting ratios and polarization purity of the beam-splitter cubes. It is therefore possible to mostly use standard commercial components. A preliminary design of the beam combiner fits on a 45 cm ×85 cm breadboard (see Figure 2.9). This compact design ensures stability and minimizes the space taken up in the beam-combination laboratory of the interferometer. Due to its high spectral resolution, the coherence length of UVES-I is very large (≥ 3 cm). However, the drift of the optical

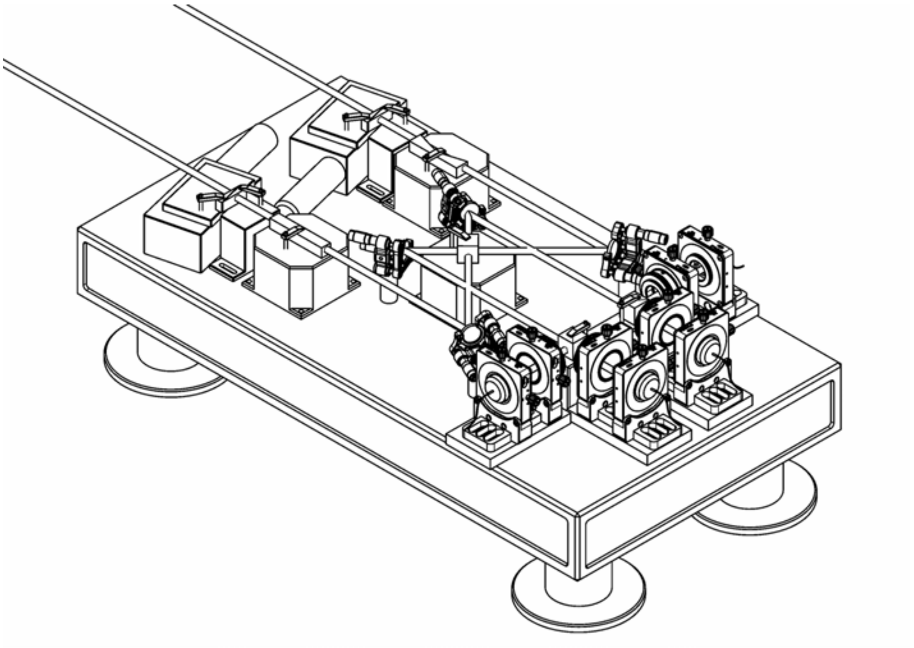

Figure 2.9 — UVES-I beam combination table. The light beams from the two telescopes enter from the top left, and pass through the atmospheric dispersion compensator and achromatic phase shifter before being combined at the central beam combiner. The two polarization states are separated, and the resulting four beams coupled into optical fibers; the four fiber holders are visible at the bottom right.

path difference *during* one exposure must not be larger than $\sim 50\,\mathrm{nm}$, as this would reduce the fringe visibility due to the fringe blurring; therefore the UVES-I breadboard should be mounted as rigidly as possible to the fringe sensing unit. This eliminates the necessity of an additional metrology system.

2.4.5 UVES instrument on UT-2

The impact of the proposed combination on the UVES instrument would be small. The UVES-I fiber interface to the spectrograph will be similar to the existing link from FLAMES (Fiber Large Array Multi Element Spectrograph) to UVES (Pasquini et al. 2000), which has a fiber head for 8 fibers. The UVES-I fiber head will be placed after the pre-slit optics and can, when UVES-I is used, be injected via a folding mirror.

To retrieve the full interferometric information only four fibers are needed. It would thus be possible to use two VLTI baselines simultaneously if an eight-fiber feed is used. This would require both of the PRIMA fringe-tracking units to stabilize the fringes on the two baselines. Interesting, but currently not possible at Paranal for an instrument like UVES-I, is the simultaneous use of three baselines, which would make it possible to measure a triangle of baselines, and aquire closure phase. For this a three-way beam combiner, with 12 output fiber is needed and the light from these fibers has to be directed on the spectrograph CCD with sufficiently-low cross-talk between the different orders.

As the light is injected via fibers into the spectrograph the spectral resolution achieved by the instrument no longer depends on the slit size, but on the core diameter of the fiber and the re-imaging optics. For example using a fiber with a core diameter of 100 μm, the fiber whose transmission is shown in Figure 2.5, and with re-imaging optics changing the F/3 fiber output beam into the F/10 beam similar to that produced by the standard pre-slit optics of UVES (Dekker et al. 2000), a spectral resolution of ~ 55000 for UVES-I would be achieved, while still making alignment of the fiber-couplers easy.

2.4.6 Performance

The detector integration times used should be sufficiently long to ensure that the detector read-noise is not dominant (see below), and sufficiently short to allow compensation of the atmospheric dispersion accumulating during the exposure with a relatively simple device (see Section 2.3.2). This will typically give exposure times between 1 min and 15 min.

The beam combiner has 12 optical surfaces (before fiber coupling). The transmissive optics will be covered with anti-reflection coatings optimized for the wavelength range used, while mirrors will be coated in protected silver. Using a conservative assumption of 95% efficiency per mirror surface and 99% efficiency per anti-reflection coated glass element, the resulting overall throughput of the beam combination table is 72%.

The transmission of the fiber link depends on the fiber coupling efficiency as well as the bulk transmission losses in the fiber. The fiber link will be similar to the fiber link of FLAMES but the fiber length will be larger, about 150 m compared to 40 m for the FLAMES-UVES link. In Figure 2.5 the transmission for 150 m of Optran Plus WF fiber is given. Note that the transmission changes from 55% to 80% between 0.6 μm and 1.0 μm

Assuming two optical surfaces at each end of the fiber couplers plus one folding mirror which can inject the light into UVES while the spectrograph is in interferometric mode, and the transmission efficiencies described above, the total transmission of the UVES-I link will vary from 45 % to 65 % over the 0.6 μm–1.0 μm wavelength band used.

The system visibility of an interferometer, i.e., the fringe contrast measured on an unresolved source, depends on the wavefront quality of the two beams and on the accuracy of overlap at the beam combiner[3]. Factors influencing the system visibility include alignment, aberrations in the instrument optics, tracking (tip-tilt) errors, and higher-order wavefront errors due to atmospheric seeing. Using tip-tilt corrected $3r_0$ apertures we expect a mean Strehl ratio of $\geq 43\%$ from each telescope (Noll 1976; Fusco & Conan 2004), providing a system visibility of order 0.40.

The total difference in sensitivity between FLAMES and the UVES-I combination depends on the instrument efficiency and the source visibility. The efficiency due to both the throughput and the system visibility would be equivalent to a loss of 10.8 magnitudes (Tab. 2.1) in both the stellar and sky background photon counts. After an integration of 2 min using the maximum spectral resolution and fast read-out rate of UVES-I, one would be in the photon-noise-limited regime for a G0 star of magnitude $R = 6$. In this regime long integrations can be constructed from multiple short exposures with no additional noise penalty in order to reach the required SNR. The signal-to-noise also varies in proportion to the source visibility. It should be pointed out that even though the sensitivity of UVES-I is significantly lower than that of UVES, the

---

[3] We do not consider the possibility of increasing the system visibility with a spatial filter here, because the introduction of such a filter would impose much more stringent requirements on the alignment and might reduce the fringe temporal stability (Tubbs 2005).

Table 2.1 — Comparison of UVES-I throughput with the throughput of UVES-FLAMES, for operation without adaptive optics (0.75 m aperture) and with adaptive optics (full 1.8 m aperture of the ATs).

Term	Flux reduction ($\frac{\mathrm{UVES-I}}{\mathrm{FLAMES}}$)
Telescope aperture area (no AO / with AO)	0.009 / 0.05
Number of telescopes	2
Transmission VLTI / UT	0.075
Beam combiner transmission	0.72
Fiber link UVES-I / FLAMES	0.75
Flux for real and imaginary components of visibility	0.5
Squared system visibility	0.16
Squared fringe tracking losses	0.85
Total (no AO / with AO)	4.9×10^{-5} / 2.8×10^{-4} 10.8mag / 8.9mag

final sensitivity compares quite favorably with other optical interferometers especially bearing in mind that the achieved spectral resolution is very high. The signal-to-noise ratio will be further reduced in proportion to the source visibility, but for many measurements described in Section 2.2 the sources need only be marginally resolved, so that the variation of visibility phase with wavelength directly probes offsets in the position of the emitting region.

For example, for a measurement of the phase change across a spectral line the adjacent continuum provides an excellent calibration, allowing measurement of phase changes with wavelength as small as one milliradian. This means that UVES-I will be sensitive to astrometric offsets that are over one hundred times smaller than the resolution limit of the interferometer. It will not be possible to image such small structures, but models of such astrometric offsets can be constructed and tested with UVES-I.

It should be pointed out that not all observing programs will require the full spectral resolution provided by the new instrument. In those cases it will be possible to obtain a higher SNR per desired spectral element by binning the data. In the readout-noise-limited regime, this can best be done on the CCD. This would have the advantage that one would be able to go to fainter targets than stated above with shorter integration times and shorter detector readout times.

Often the astrophysical interesting signal is encoded in multiple lines in a spectral region (Section 2.2). In this case the SNR can be improved by cross-correlating these absorption lines with a line-template mask. This is routinely done in high-resolution spectroscopy, (e.g. Griffin 1967; Queloz 1995; Donati et al. 1997; Rucinski 1999) but has not yet been done with optical interferometers, while it would be possible with an instrument like UVES-I.

2.5 Other interferometer-spectrograph pairings

In this section we give some remarks about other possible pairings of interferometers and spectrographs at different sites and in different wavelength regimes.

The high-resolution spectrograph CRIRES at Paranal Observatory covers the wavelength range from 1 μm to 5 μm and has a spectral resolution up to $R_{CRIRES} \sim 10^5$ (Kaeufl et al. 2004). The wavelength range would overlap with the wavelength range of AMBER (Petrov et al. 2003) but with a much higher resolution ($R_{AMBER} \sim 12000$). The throughput of the VLTI+CRIRES combination would be higher than UVES-I as the transmission of the VLTI increases towards longer wavelengths. The distortions of the incoming wavefronts are also less severe for the longer wavelengths (see Section 2.3.1), so one would be able to use the full aperture of the ATs or make observations with the UTs using the MACAO AO system (Arsenault et al. 2004). For a combination of CRIRES with the VLTI one could use the Optran Plus WF fiber (Figure 2.5) as the transmission for a 150 m of Optran Plus WF fiber between 1 μm and 2 μm would be $\sim$ 80 %. Note the dip at $\sim$ 2 μm and the steep decline in transmission beyond 2 μm.

In the Northern hemisphere the Mauna Kea Observatory site would be well-suited for the high spectral resolution optical/IR interferometer design advocated in this chapter. The Keck interferometer (KI) is already in place at the observatory and its infrastructure is similar to the one found at the VLTI (delay lines, 2-μm fringe tracker). The HIRES spectrograph with the spectral range from 0.3 μm to 1.1 μm and a resolving power of $R \sim 67000$ (Vogt et al. 1994) at the Keck I Telescope covers a similar wavelength-range to the UVES spectrograph. Therefore a similar approach as described in Section 2.4 is possible for mating HIRES and KI. The combination of a high-resolution spectrograph with an interferometer at this site seems particular attractive from the scientific point of view, as so far the interferometer has no spectrographic mode.

A second interferometer, the OHANA experiment, is also currently being set up at Mauna Kea (Perrin et al. 2004). This instrument uses optical fibers for beam transport instead of the bulk optics used in conventional interferometers. This allows combination of telescopes which were not originally designed for interferometry, forming an array several hundred meters across. Using the OHANA array, one would potentially have access to all spectrographs at the telescopes which are connected to OHANA. However one has to use the bandwidth offered by the OHANA fibers (J,H,K). One would prefer to keep the length of the transport of the beams after the combination in the interferometric lab short to avoid unnecessary losses, therefore one could use the spectrographs at the telescope where the beam combiner is placed. A new beam combiner at CFHT will be used by the OHANA project in addition to the existing K-band fringe tracker on the Keck Interferometer. The Near Infrared Echelle Spectrograph (NIRSPEC) at the Keck II could be used as the spectrograph.

2.6 Conclusion

This article shows that the combination of high-resolution spectroscopy with long-baseline interferometry gives access to hitherto unobservable properties of stellar surfaces and circumstellar matter.

Furthermore the article shows how this combination can be achieved without building a major new instrument; only a beam combiner and a fiber link are needed. No instrument components are required which would be expensive or time-consuming to make. The use of external fringe tracking is essential for an instrument like this as it enables long integration times. Time-varying longitudinal dispersion could severely limit the possibilities of such an instrument. Dispersion compensation techniques are investigated in this article and a solution is presented which allows integration times up to a few minutes.

The implementation of this approach is shown for the example combination UVES-VLTI. The resulting instrument would differ from other instruments or efforts taken to achieve high spatial and spectral resolution. It would offer spectral resolution nearly a factor 2 higher than for any other interferometric instrument, and over a wide spectral range of a few hundred rather than a few tens of nanometers. It offers the same possibilities to an astronomer as a high-resolution Echelle spectrograph behind a single telescope does, plus the high spatial resolution due to the interferometer, albeit only for bright targets. However it is important to realize that this concept, the combination of two existing instruments to create a new one, is not limited to a specific location or instrument, but rather is an approach which can be followed at different observatories in both hemispheres.

It is worth pointing out that the measurements taken with the proposed instruments are differential in nature (e.g. change of visibility amplitude and visibility phase over spectral lines), allowing many interferometric calibration problems to be circumvented. As noted in Section 2.2, these differential measurements contain a wealth of astronomical information in the optical/IR regime.

Acknowledgments

We are thankful to Jeff Meisner, Luca Pasquini, and Gerardo Avila for many useful discussions and suggestions. We are grateful to Richard J. Mathar for providing material on the refractivity of water vapor.

Bibliography

Albrecht, S., Bakker, E. J., de Jong, J. A., et al. 2004, in Proc. SPIE, ed. W. A. Traub, Vol. 5491, 1266 21, 26

Arsenault, R., Donaldson, R., Dupuy, C., et al. 2004, in Proc. SPIE, ed. D. Bonaccini Calia, B. L. Ellerbroek, & R. Ragazzoni, Vol. 5490, 47 32

Berger, D. H., ten Brummelaar, T. A., Bagnuolo, Jr., W. G., & McAlister, H. A. 2003, in Proc. SPIE, ed. W. A. Traub, Vol. 4838, 974 27

Buscher, D. F., Armstrong, J. T., Hummel, C. A., et al. 1995, Appl. Opt., 34, 1081 24

Chelli, A. & Petrov, R. G. 1995, A&AS, 109, 401 15

Ciddor, P. E. 1996, Appl. Opt., 35, 1566 26

Colavita, M. M., Wizinowich, P. L., & Akeson, R. L. 2004, in Proc. SPIE, ed. W. A. Traub, Vol. 5491, 454 21

Cunha, M. S., Aerts, C., Christensen-Dalsgaard, J., et al. 2007, A&A Rev., 14, 217 15

Dekker, H., D'Odorico, S., Kaufer, A., Delabre, B., & Kotzlowski, H. 2000, in Proc. SPIE, ed. M. Iye & A. F. Moorwood, Vol. 4008, 534 30

Delplancke, F. 2003, PRIMA, the Phase Referenced Imaging and Microarcsecond Astrometry facility: High Level Requirements & System Description, ESO Doc. ref.: VLT-SPE-ESO-15700-3051 21, 27

Domiciano de Souza, A., Zorec, J., Jankov, S., et al. 2004, A&A, 418, 781 15, 16

Donati, J.-F., Semel, M., Carter, B. D., Rees, D. E., & Collier Cameron, A. 1997, MNRAS, 291, 658 31

Fried, D. L. 1966, Optical Society of America Journal, 56, 1372 17

Frink, S., Mitchell, D. S., Quirrenbach, A., et al. 2002, ApJ, 576, 478 15

Fusco, T. & Conan, J.-M. 2004, Journal of the Optical Society of America A, 21, 1277 30

Goodman, J. W. 1985, Statistical Optics, Chapter 8 (Wiley) 24

Gray, D. F. 1977, ApJ, 211, 198 16

Griffin, R. F. 1967, ApJ, 148, 465 31

Jankov, S., Vakili, F., Domiciano de Souza, Jr., A., & Janot-Pacheco, E. 2002, in ASP Conference Series, Vol. 259, IAU Colloq. 185: Radial and Nonradial Pulsationsn as Probes of Stellar Physics, ed. C. Aerts, T. R. Bedding, & J. Christensen-Dalsgaard, 172 14

Kaeufl, H.-U., Ballester, P., Biereichel, P., et al. 2004, in Proc. SPIE, ed. A. F. M. Moorwood & M. Iye, Vol. 5492, 1218 32

Kochukhov, O., Drake, N. A., Piskunov, N., & de la Reza, R. 2004, A&A, 424, 935 14

Kolmogorov, A. 1941, Akademiia Nauk SSSR Doklady, 30, 301 17

Labeyrie, A. 1975, ApJ, 196, L71 22

Lin, D. N. C. & Ida, S. 1997, ApJ, 477, 781 16

Lucke, R. L. & Young, C. Y. 2007, Appl. Opt., 46, 559 24

Marengo, M., Sasselov, D. D., Karovska, M., Papaliolios, C., & Armstrong, J. T. 2002, ApJ, 567, 1131 15

Martin, F., Conan, R., Tokovinin, A., et al. 2000, A&AS, 144, 39 25

Mathar, R. J. 2004, Appl. Opt., 43, 928 26

McAlister, H. A., Ten Brummelaar, T. A., Aufdenberg, J. P., et al. 2004, in Proc. SPIE, ed. W. A. Traub, Vol. 5491, 472 21

Meilland, A., Stee, P., Vannier, M., et al. 2007, A&A, 464, 59 16

Meisner, J. A. 2007, Using the FSU to generate a phase reference for coherent integration by MIDI at N band, Unpublished 25, 26

Monnier, J. D. 2003, Reports of Progress in Physics, 66, 789 17

Nagasawa, M., Ida, S., & Bessho, T. 2008, ApJ, 678, 498 16

Nardetto, N., Mourard, D., Mathias, P., & Fokin, A. 2006, Memorie della Societa Astronomica Italiana, 77, 235 15

Noll, R. J. 1976, Optical Society of America Journal, 66, 207 30

Papaloizou, J. C. B. & Terquem, C. 2001, MNRAS, 325, 221 16

Pasquini, L., Avila, G., Allaert, E., et al. 2000, in Proc. SPIE, ed. M. Iye & A. F. Moorwood, Vol. 4008, 129 29

Perrin, G. S., Lai, O., Woillez, J. M., et al. 2004, in Proc. SPIE, ed. W. A. Traub, Vol. 5491, 391 32

Petrov, R. G. 1989, in NATO ASIC Proc. 274: Diffraction-Limited Imaging with Very Large Telescopes, ed. D. M. Alloin & J.-M. Mariotti, 249 15

Petrov, R. G., Malbet, F., Weigelt, G., et al. 2003, in Proc. SPIE, ed. W. A. Traub, Vol. 4838, 924 32

Puech, F. & Gitton, P. 2006, Interface Control Document between VLTI and its Instruments, ESO Doc. ref.: VLT-ICD-ESO-15000-1826 24

Queloz, D. 1995, in IAU Symposium, Vol. 167, New Developments in Array Technology and Applications, ed. A. G. D. Philip, B. Hauck, & A. R. Upgren, 221 31

Quirrenbach, A. 2001, ARA&A, 39, 353 14, 21

Quirrenbach, A. & Aufdenberg, J. 2003, in IAU Symposium, Vol. 210, Modelling of Stellar Atmospheres, ed. N. Piskunov, W. W. Weiss, & D. F. Gray, 68P 13

Quirrenbach, A., Bjorkman, K. S., Bjorkman, J. E., et al. 1997, ApJ, 479, 477 16

Quirrenbach, A., Mozurkewich, D., Armstrong, J. T., Buscher, D. F., & Hummel, C. A. 1993, ApJ, 406, 215 13

Rice, J. B. 2002, Astronomische Nachrichten, 323, 220 14

Roddier, F. 1981, Prog. Optics, 19, 281 17

Rucinski, S. 1999, in ASP Conference Series, Vol. 185, IAU Colloq. 170: Precise Stellar Radial Velocities, ed. J. B. Hearnshaw & C. D. Scarfe, 82 31

Sabbey, C. N., Sasselov, D. D., Fieldus, M. S., et al. 1995, ApJ, 446, 250 15

Shao, M., Colavita, M. M., Hines, B. E., Staelin, D. H., & Hutter, D. J. 1988, A&A, 193, 357 22

Shulyak, D., Tsymbal, V., Ryabchikova, T., Stütz, C., & Weiss, W. W. 2004, A&A, 428, 993 14

Tatarski, V. I. 1961, Wave Propagation in a Turbulent Medium (McGraw-Hill) 17

Taylor, G. I. 1938, in Proceedings of the Royal Society of London A, 164, 476 24

Tsuji, T. 2006, ApJ, 645, 1448 14

Tubbs, R. 2005, Appl. Opt., 44, 6253 30

Tubbs, R. N., Launhardt, R., Meisner, R., & Mathar, R. 2007, ESPRI Exoplanets Search with PRIma: Astrometric Error Budget, ESO Doc. ref.: VLT-TRE-AOS-15753-0001, V2.1 27, 28

Tuthill, P. G., Haniff, C. A., & Baldwin, J. E. 1999, MNRAS, 306, 353 14

Tycner, C., Gilbreath, G. C., Zavala, R. T., et al. 2006, AJ, 131, 2710 16

Vakili, F., Mourard, D., Stee, P., et al. 1998, A&A, 335, 261 12

Vogt, S. S., Allen, S. L., Bigelow, B. C., et al. 1994, in Proc. SPIE, ed. D. L. Crawford & E. R. Craine, Vol. 2198, 362 32

Weigelt, G., Kraus, S., Driebe, T., et al. 2007, A&A, 464, 87 12

Wittkowski, M., Aufdenberg, J. P., Driebe, T., et al. 2006, A&A, 460, 855 14

Wu, Y. & Murray, N. 2003, ApJ, 589, 605 16

Young, J. S., Baldwin, J. E., Basden, A. G., et al. 2003, in Proc. SPIE, ed. W. A. Traub, Vol. 4838, 369 14, 16